Bistatic RCS Calculations with the Vector Parabolic Equation Method

Andrew A. Zaporozhets and Mireille F. Levy, *Senior Member, IEEE*

***Abstract*—The vector parabolic equation (PE) method provides accurate solutions for electromagnetic scattering from three-dimensional (3-D) objects ranging from a size comparable to the wavelength of the incident wave to several tens of wavelengths. A paraxial version of Maxwell's equations is solved with a marching solution that only requires limited computing resources, even for large scatterers. By decoupling the PE paraxial direction from the direction of incidence, the bistatic radar cross section (RCS) can be computed at all scattering angles. A sparse-matrix formulation is used to implement electromagnetic boundary conditions, ensuring that polarization effects are treated fully. Computing costs are kept to a minimum through the use of a double-pass method so that calculations can be carried out on a desktop computer for realistic targets and radar frequencies. The method has been validated on simple canonical shapes and tested on complex targets.**

***Index Terms*— Electromagnetic scattering, parabolic equation method, radar cross section.**

I. Introduction

PARABOLIC equation (PE) techniques have been used for some time to solve long-range forward propagation problems for radar and sonar applications [1], [2]. More recently, they have been applied to scattering problems and, in particular, to radar cross section (RCS) calculations [3], [4]. The approach of [3], [4] gave very encouraging results, but could not provide the full bistatic scattering pattern of a target because of intrinsic paraxial limitations.

In a recent publication [5] on acoustic scattering, it was shown that these paraxial limitations of the PE method can be lifted to a large extent by decoupling the paraxial direction from that of the incident wave and solving for the scattered field rather than the total field. In this paper, we develop a paraxial framework for Maxwell's equations in order to treat polarization effects fully for electromagnetic scattering. We then apply the rotating PE method of [5] to obtain bistatic scattering results at all scattering angles. The resulting vector PE algorithms provide an efficient numerical technique, which is somehow intermediate between rigorous solutions like the method of moments [6] or FDTD methods [7] and facet-based approximations involving physical optics and the physical theory of diffraction [8]. The field scattered by three-dimensional (3-D) objects ranging in size from a wavelength or so to several tens or even hundreds of wavelengths can be calculated on a desktop computer.

The PE framework is presented in Section II and the vector PE formulation is given in Section III. Implementation topics are considered in Section IV. Section V outlines near-field/far-field transformations in the PE framework. Finally, a number of examples are presented in Section VI.

II. Parabolic Equation Framework for Scattering Applications

In all that follows, we assume $\exp(-i\omega t)$ time dependence of the fields. Working with Cartesian coordinates (x, y, z), we introduce the reduced function associated with a field component ψ

$$u(x, y, z) = \exp(-ikx)\psi(x, y, z). \tag{1}$$

This definition of u is linked to the choice of the x-direction as the paraxial direction. The reduced function is slowly varying in range for energy propagating close to the paraxial direction, which gives it convenient numerical properties. We shall not recall the derivation of the outgoing parabolic equation, which can be found in [2] for example. Basically, the scalar wave equation is split into two parabolic terms, one representing energy propagating in the forward paraxial cone (increasing x) and the other the backward propagating energy (decreasing x). The outgoing parabolic equation for u is

$$\frac{\partial u}{\partial x} = -ik(1 - Q)u \tag{2}$$

where the pseudodifferential operator Q is defined by

$$Q = \sqrt{\frac{1}{k^2}\frac{\partial^2}{\partial y^2} + \frac{1}{k^2}\frac{\partial^2}{\partial z^2} + n^2(x, y, z)}. \tag{3}$$

The great advantage of (2) is that it can be marched in range, getting the solution at range $x + \Delta x$ from that at range x and suitable boundary conditions on the scattering object and at the outer boundaries of the integration domain, as shown in Fig. 1. The main limitation is that the square-root operator can only be defined in a paraxial cone, so that a single PE run can only give a partial image of scattering phenomena. We shall see below that it is possible to overcome this restriction by carrying out several "rotated" PE runs to cover all scattering angles of interest.

PE techniques are not restricted to forward scatter. The first approach in building up a more complete picture consists in computing the backscattered field by treating scattering objects

Manuscript received November 11, 1997; revised May 28, 1999. This work was supported by the Radiocommunications Agency, Department of Trade and Industry, and by the Engineering and Physical Sciences Research Council, U.K.

The authors are with the Rutherford Appleton Laboratory, Chilton, Didcot, Oxfordshire, OX11 0QX U.K.

Publisher Item Identifier S 0018-926X(99)09948-2.

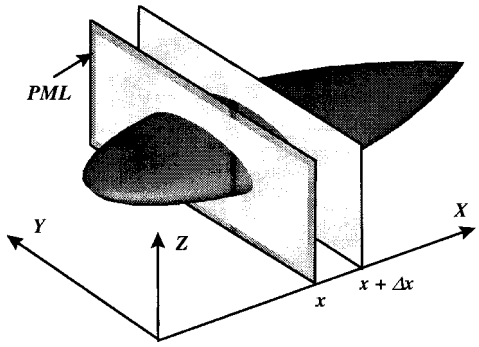

Fig. 1. Basic geometry for PE marching. The integration domain in the transverse plane is truncated with the perfectly matched layer (PML) method.

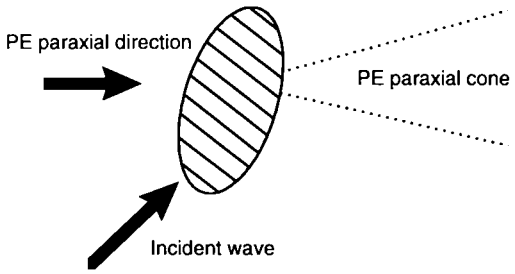

Fig. 2. Rotation of the PE paraxial direction.

as a sequence of reflecting facets [3]. Starting with the field set to zero on a transverse plane beyond the scatterer, the solution is marched back adding the new facet sources at each step with appropriate boundary conditions. This technique provided very encouraging results for both forward and backscatter. Its major drawback is that it cannot be used to compute the scattered field at 90° from the incident direction since this is in the region forbidden to the paraxial approximation.

A new ingredient is necessary in order to lift this restriction. The solution is to solve for the *scattered* field directly rather than for the total field [5]. We write

$$\psi^t = \psi^i + \psi^s \tag{4}$$

where ψ^t, ψ^i, and ψ^s are the total, incident and scattered fields, respectively. Outside the scattering objects, all three satisfy the wave equation. We now consider the reduced scattered field $u^s = e^{-ikx}\psi^s$ and solve for the part of $u^{s,x}$ of u^s which propagates in a paraxial cone centred on the positive x-direction. This function will satisfy the outgoing parabolic equation (2). With this procedure, the direction x is arbitrary and need not be linked to that of the incident wave. With a single PE run, we can cover a sector centred on a given scattering direction. By rotating the paraxial direction and repeating this process, we can reconstruct the scattered field everywhere. Fig. 2 illustrates the decoupling of incident and paraxial directions which is central to the rotating PE method. Since we solve the PE for the scattered field, one might wonder how the incident field is taken into account. The answer is given by the boundary conditions on the scatterer, which become nonhomogeneous as they must now refer to the incident field. A slightly surprising consequence of solving for the scattered field is that the initial field for the marching algorithm should be zero: since integration starts on a transverse plane before the scatterer, the scattered field there cannot have any forward propagating components. Indeed $u^{s,x}$ is zero until the boundary of the scatterer is reached, at which point the nonhomogeneous boundary conditions introduce the scattering sources into the marching solution.

In the rest of this paper, we assume a homogeneous background medium, taking n constant equal to 1 as is customary for RCS calculations. In this work, we use the simplest approximation of (2), which is obtained with first order Taylor expansions of the square root and the exponential. This yields the well-known standard parabolic equation (SPE)

$$\frac{\partial u}{\partial x} = \frac{i}{2k}\left(\frac{\partial^2 u}{\partial y^2} + \frac{\partial^2 u}{\partial z^2}\right). \tag{5}$$

The SPE is a narrow-angle approximation, which is very accurate at angles within 15° or so of the paraxial direction (the positive direction of the x-axis). In geometrical optics (GO) terms this means that SPE support rays traveling within a 15° cone around the x-axis. Because of the simplicity of the SPE, boundary conditions on the scatterer are relatively easy to incorporate, which we found particularly useful for 3-D electromagnetic applications where coding can become quite intricate.

We should state here that the narrow-angle approximation is only accurate when energy scattered by the object does not undergo large changes in direction. This can break down for nonconvex objects [5] and cavities. A much more fundamental difficulty is that for objects which are small compared to the wavelength, creeping waves can travel all the way around the scatterer. Second-time-around creeping waves cannot be captured by the rotating PE method. Some kind of an iterative technique, probably based on a combination of forward/backward PE runs and application of the wide-angle PE schemes, which are accurate up to 90° of the paraxial direction [9], would be required to model them accurately. The performance of the rotating PE on small objects will be discussed further in Section VI.

III. Vector Parabolic Equation

We now turn to the problem of linking scalar wave equations to electromagnetic field components. We denote the electric and magnetic fields by $\mathbf{E} = (E_x, E_y, E_z)$ and $\mathbf{H} = (H_x, H_y, H_z)$, respectively. For two-dimensional (2-D) problems when the fields are independent of the transverse coordinate y, the simplest option is to take is

$$\begin{cases} \psi = E_y, & \text{for horizontal polarization} \\ \psi = H_y, & \text{for vertical polarization.} \end{cases}$$

The determination of ψ suffices to solve the whole electromagnetic problem: by using the curl equations, all field components are determined and they automatically satisfy the divergence-free conditions.

The situation is, of course, different in three dimensions. Some additional effort is then required to get a solution

satisfying Maxwell's equations. First, we obtain a scalar wave equation for each electromagnetic field component from the curl equations. Second, these component scalar wave equations are coupled through boundary conditions on the scattering object and through the divergence-free condition in order to obtain a well-determined system. In this work, we only examine the case of perfectly conducting scatterers. Then boundary conditions on the object can be written in terms of the electric field only, so that we have a self-contained system of equations to solve for the electric field. The magnetic field can be obtained through the curl equation if required. For a perfect conductor, the tangential electric field must be zero on the object or, equivalently, the electric field must be parallel to the normal. This gives the following system of equations:

$$\begin{cases} n_x E_y(P) - n_y E_z(P) = 0 \\ n_x E_z(P) - n_z E_x(P) = 0 \\ n_y E_x(P) - n_x E_y(P) = 0 \end{cases} \tag{6}$$

where P is a point on the surface of the scatterer and $\vec{n} = (n_x, n_y, n_z)$ is the outer normal to the surface at P. In terms of the PE reduced scattered field, these conditions become nonhomogeneous. For example the first equation of (6) is written as

$$n_x u_y^s(P) - n_y u_z^s(P) = -e^{ikx}(n_x E_y^i(P) - n_y E_z^i(P)) \tag{7}$$

where (E_x^i, E_y^i, E_z^i) is the incident electric field.

The three equations in (6) are not independent, but form a system of rank 2. Hence, we need another equation to ensure unicity of the solution. This is provided by the divergence-free condition of Maxwell's equations

$$\frac{\partial E_x^s}{\partial x} + \frac{\partial E_y^s}{\partial y} + \frac{\partial E_z^s}{\partial z} = 0 \tag{8}$$

where (E_x^s, E_y^s, E_z^s) is the scattered electric field. It should be noted here that in the 2-D case the fields are automatically divergence-free since we solve for E_y^s or H_y^s, which do not depend on y. This is no longer true in the 3-D case, where the divergence-free condition must be enforced explicitly. Enforcing the divergence-free condition on the object boundary ensures a well-determined system of equations, and we show in the Appendix that the PE solution is then divergence-free everywhere. The parabolic equation formulation avoids the need for direct estimation of the range derivatives in the divergence-free condition, yielding an expression involving points in the transverse plane only. We can rewrite (8) as

$$\frac{i}{2k}\left(\frac{\partial^2 u_x^s}{\partial y^2} + \frac{\partial^2 u_x^s}{\partial z^2}\right) + iku_x^s + \frac{\partial u_y^s}{\partial y} + \frac{\partial u_z^s}{\partial z} = 0. \tag{9}$$

IV. Implementation Aspects

The finite-difference scheme used to solve the coupled system of parabolic equations has been described in [5]. Scattering objects are discretized on a rectangular grid, keeping track of the normal along the surface of the scatterer. The grid spacing is fixed in the transverse $(y$-$z)$ plane, but adaptive in range. Since the nonhomogeneous boundary conditions contain an exponential term in x on the right-hand side [see (7) for example], accurate representation of phase variations require smaller grid spacing as the angle between the paraxial and incident directions increases. Typical range steps are 1/10th of a wavelength or less. This situation is totally different from that of long-range radiowave propagation PE codes, where range steps are usually several order of magnitude larger than the wavelengths. However, the small range steps necessary for scattering PE applications do not lead to major computing difficulties since for most RCS applications target dimensions are less than a few hundred wavelengths.

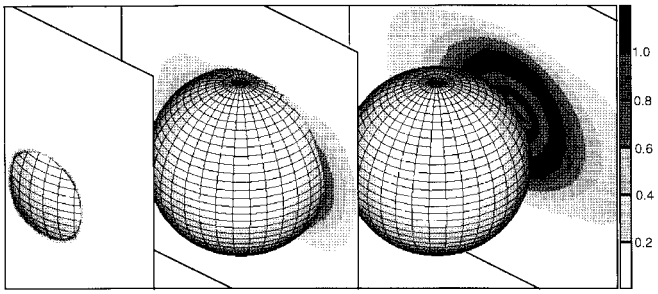

Fig. 3. Scattering by perfectly conducting sphere of radius 5λ, showing the amplitude of the vertical component of the scattered electric field as it propagates. The incident wave has vertical polarization.

For domain truncation in the transverse plane, we selected the perfectly matched layer (PML) technique [10], which has recently been adapted for paraxial methods [11]. This is straightforward to implement with a narrow-angle PE code and very efficient computationally, as only a few grid-points are necessary to absorb unwanted energy.

In 2-D applications, finite-difference PE schemes can be written in terms of tridiagonal matrices that are straightforward to invert [3]. Because of the coupling of scalar components through nonseparable boundary conditions, this is no longer the case for 3-D applications. Each step now requires the inversion of a sparse matrix. Computation times in three dimensions would be prohibitive if the sparse matrix solver was used in the whole transverse domain. Instead, we use a double-pass method, where the field is first propagated assuming the object is not present at the next range [5]. For this first pass the equations are separable and the scheme can be factored into tridiagonal matrices, which can be inverted efficiently with Gauss pivot methods. In the second pass, the field is recalculated taking the object into account, using the first pass results as boundary values for a small transverse region enclosing the scatterer. A sparse matrix formulation implementing the electromagnetic boundary conditions is used for this second pass, ensuring that polarization effects are fully taken into account.

Integration starts just before the scatterer and is normally stopped just beyond the scatterer since far-field results can then be obtained through Fourier transforms as explained in the next section. Fig. 3 shows the vertical component of the scattered electric field as it propagates along a metallic sphere of radius 5λ, where the incident field is a vertically polarized plane wave of wavelength λ. We should emphasize here that the near-field calculated by the narrow-angle PE method only contains energy propagating at small angles from the paraxial direction and, hence, is not an accurate representation of the

actual near field. This does not affect the quality of the far-field results, as discussed in Section VI.

Typical integration times for a single rotating PE run on a 133-MHz Pentium are of the order of a few minutes for 3-D simulations of forward scatter. Timings increase with the angle between paraxial and incident directions, and can reach several hours for backscatter calculations. If bistatic RCS results are required at scattering angles encompassing several narrow-angle sectors, an appropriate number of runs is carried out and the scattering pattern is constructed by using the relevant results in each sector.

V. Far-Field Formulas

The field at larger distances can be derived from near-field computations by solving the PE in closed form in vacuum. Expressions for the 2-D case can be found in [3]. In three dimensions, the paraxial far-field formula involves an exponential convolution kernel

$$\psi^s(x,y,z) = -\frac{1}{2\pi}\int_{-\infty}^{\infty}\int \psi^s(x_0,y',z') \times \left[ik\frac{(x-x_0)}{d(y',z')} - \frac{1}{d(y',z')}\right] \cdot \frac{e^{ikd(y',z')}}{d(y',z')}\,dy'\,dz' \tag{10}$$

where $d(y',z') = \sqrt{(x_0-x')^2+(y-y')^2+(z-z'^2}$. For brevity's sake, we omit the proof of (10), which involves plane wave decomposition techniques. By letting the observation point tend to infinity in a given direction, we get the bistatic RCS. The total bistatic RCS in direction (θ,φ) is defined as

$$\sigma(\theta,\varphi) = \lim_{r\to\infty} 4\pi r^2 \frac{|\mathbf{E}^s(x,y,z)|^2}{|\mathbf{E}^i(x,y,z)|^2} \tag{11}$$

where $x = r\cos\theta$, $y = r\sin\theta\cos\varphi$, $z = r\sin\theta\sin\varphi$.

In many examples, receiver polarization has to be taken into account. The quantity of interest is then the bistatic RCS in direction (θ,φ) assuming receiver polarization along vector $\mathbf{t}$, which is given by

$$\sigma_{bft}(\theta,\varphi) = \lim_{r\to\infty} 4\pi r^2 \frac{|\mathbf{E}^s(z,y,z)\cdot\mathbf{t}|^2}{|\mathbf{E}^i(x,y,z)|^2}. \tag{12}$$

If the incident field is a plane wave with unit amplitude, the RCS in direction (θ,φ) along polarization $\mathbf{t}$ derived from (10) is given by

$$\sigma_{\mathbf{t}}(\theta,\varphi) = \frac{k^2\cos^2\theta}{\pi}\left|\int_{-\infty}^{\infty}\int_{-\infty}^{\infty}(\mathbf{E}^s(x_0,y',z')\cdot\mathbf{t}) \cdot e^{-ik\sin\theta(y'\cos\varphi+z'\sin\varphi)}\,dy'\,dz'\right|^2. \tag{13}$$

This formula can of course be used to calculate cross and copolarized cross sections by using the appropriate transmitter and receiver polarization's. It is also used to compute the total bistatic RCS by summing the x,y, and z components of the RCS.

These expressions show that the bistatic RCS is obtained as the Fourier transform of the field in any transverse plane located beyond the object. With the very small integration domains used here, it is not worth using fast Fourier transforms. Instead, we compute the integrals directly with a standard Simpson scheme.

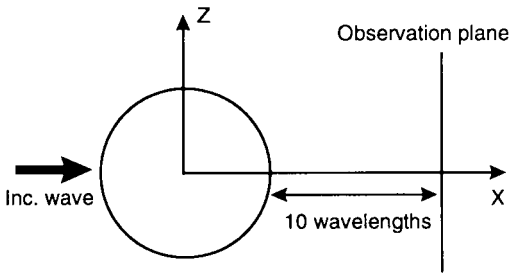

Fig. 4. Geometry for scattering by circular cylinder.

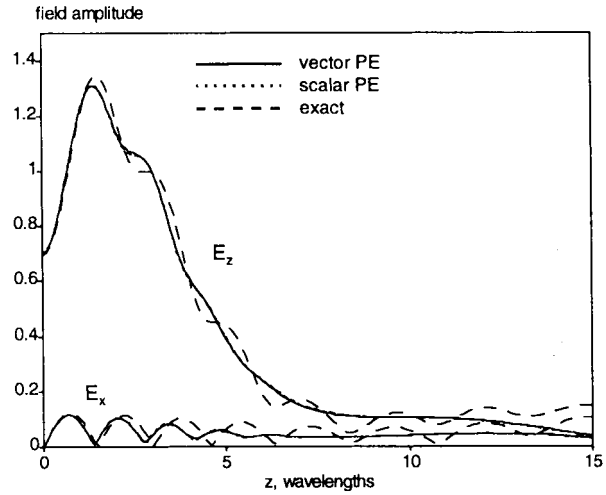

Fig. 5. Near-field results for perfectly conducting circular cylinder for vertically polarized incident field. The dotted line (scalar PE result) is almost identical to the solid line (vector PE result).

VI. Examples

We start with a simple validation of the vector PE formulation on a 2-D example. A vertically polarized plane wave of wavelength λ is incident on a perfectly conducting circular cylinder of radius 5λ, as shown in Fig. 4. We can either solve for the magnetic field H_y with the scalar PE or the electric field components E_x, E_z with the vector PE. Fig. 5 shows forward scatter results in a transverse plane located 10λ beyond the cylinder. For this 2-D test, we used a standard narrow-angle code for the scalar PE and a single-pass full matrix inversion code for the vector PE. The E_x, E_z scalar PE results have been calculated by numerical differentiation of H_y. The scalar and vector PE results are almost identical. For comparison, we also show analytical results computed from a Hankel and cosine functions expansion [12]. These

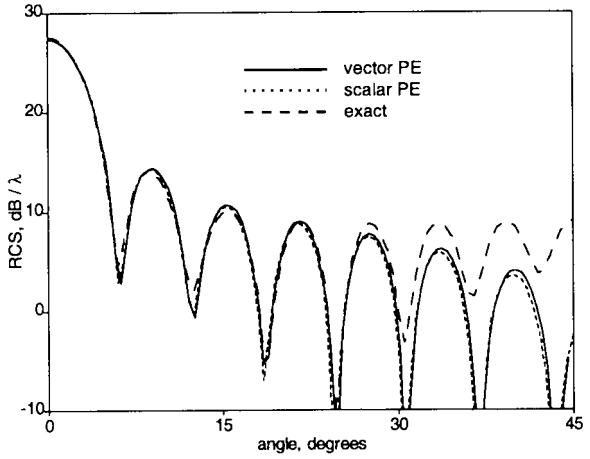

Fig. 6. Bistatic RCS of circular cylinder of radius 5λ from single PE run.

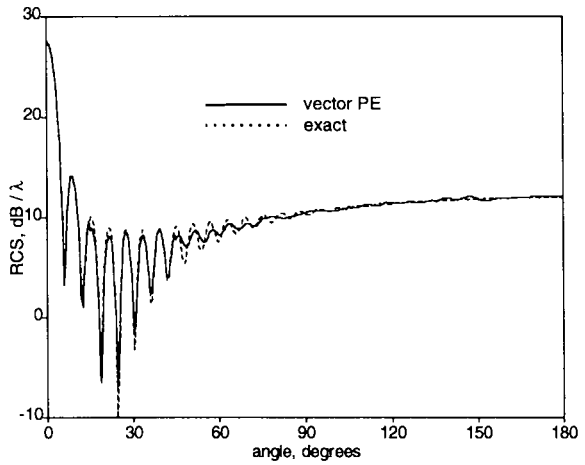

Fig. 7. Bistatic RCS of circular cylinder of radius 5λ from seven rotated vector PE runs.

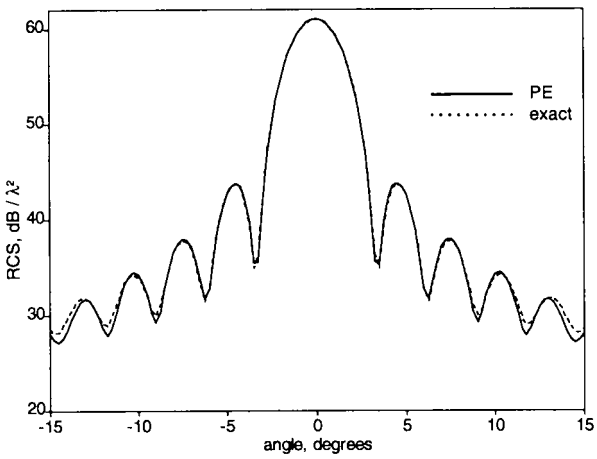

(a)

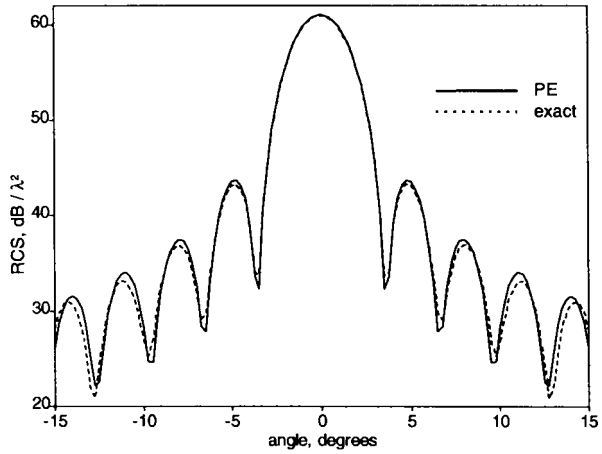

(b)

Fig. 8. Total bistatic RCS for perfectly conducting sphere of radius 10λ from single forward scatter vector PE run. (a) Horizontal plane pattern. (b) Vertical plane pattern.

differ substantially from the PE results. The reason for this is that the near-field narrow-angle PE results do not represent large angle diffraction accurately; in particular, interference between the fields diffracted from the top and bottom of the cylinder is incorrectly modeled. Fig. 6 shows the bistatic RCS results obtained from the three methods for angles up to 45°, assuming a wavelength of 1 m. Here, agreement is very good for scattering angles up to 25° or so, showing that the imperfect near-field results contain the correct small angle propagation components. In order to obtain the full bistatic RCS pattern, the paraxial direction has to be rotated in 30° steps. Fig. 7 shows the combined RCS pattern obtained with the vector PE together with the analytical solution. Agreement is excellent over the whole angular range. In all figures in this paper, the angle is measured from the direction of the incident wave.

We now look at scattering by perfectly conducting spheres. The vector PE solution is compared to the theoretical solution given by Mie expansions [12]. Fig. 8 shows forward scatter results for a single PE run for a sphere of radius 10λ for both horizontal and vertical plane patterns, assuming a wavelength of 0.1 m (frequency 3 GHz). Agreement with the theory is very good, particularly for the horizontal plane pattern, where oscillations are less marked. The error increases toward the larger angles, as the accuracy of the narrow-angle PE approximation decreases. It should be noted here that this case would be quite stressful for a full wave method like the methods of moments in view of the large size of the object. The PE execution time was under 10 min on a 133-MHz Pentium machine.

Fig. 9 shows the full bistatic scattering pattern for a sphere of radius 5λ. Again, both the vector PE and the theoretical results are shown. For each plane, the full pattern required seven PE runs covering angular sectors of 30° each. Since the larger scattering angles require finer grids, computation times increase as the paraxial direction moves toward 180°. The longest execution time was 2 h. The complete execution time was about 6 h per plane pattern. Agreement with the theoretical results is excellent for this case, which would be computer-intensive for method of moment codes.

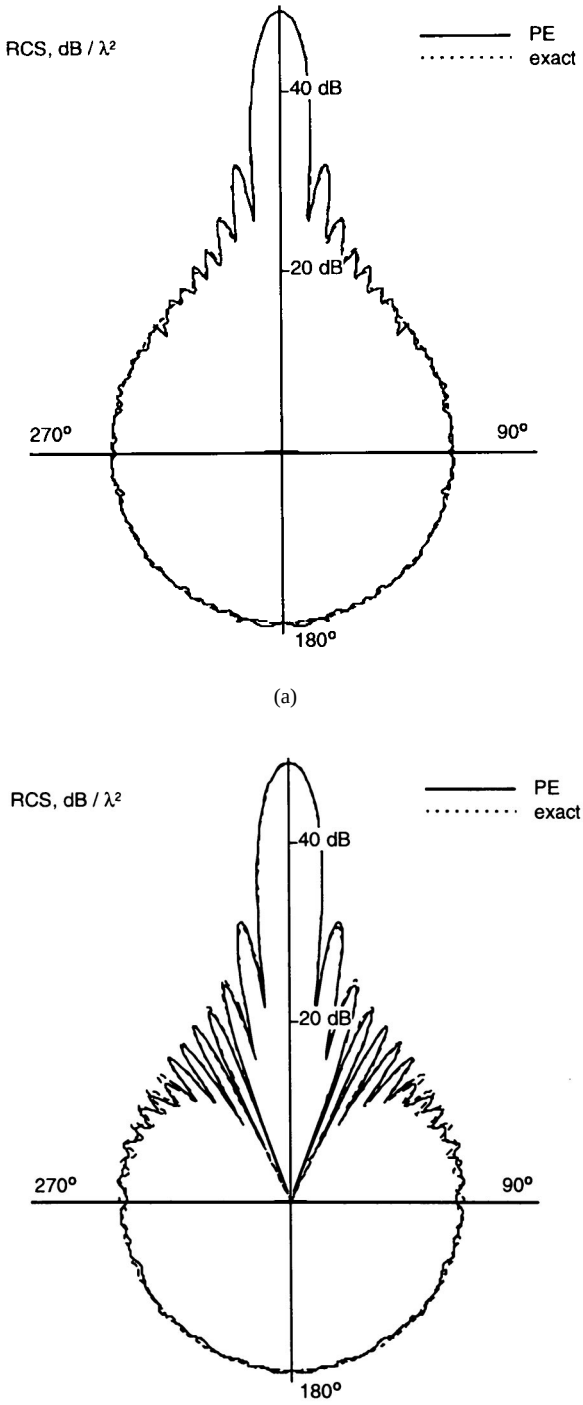

Fig. 9. Total bistatic RCS for a perfectly conducting sphere of radius 5λ from seven rotated vector PE runs. (a) Horizontal plane pattern. (b) Vertical plane pattern.

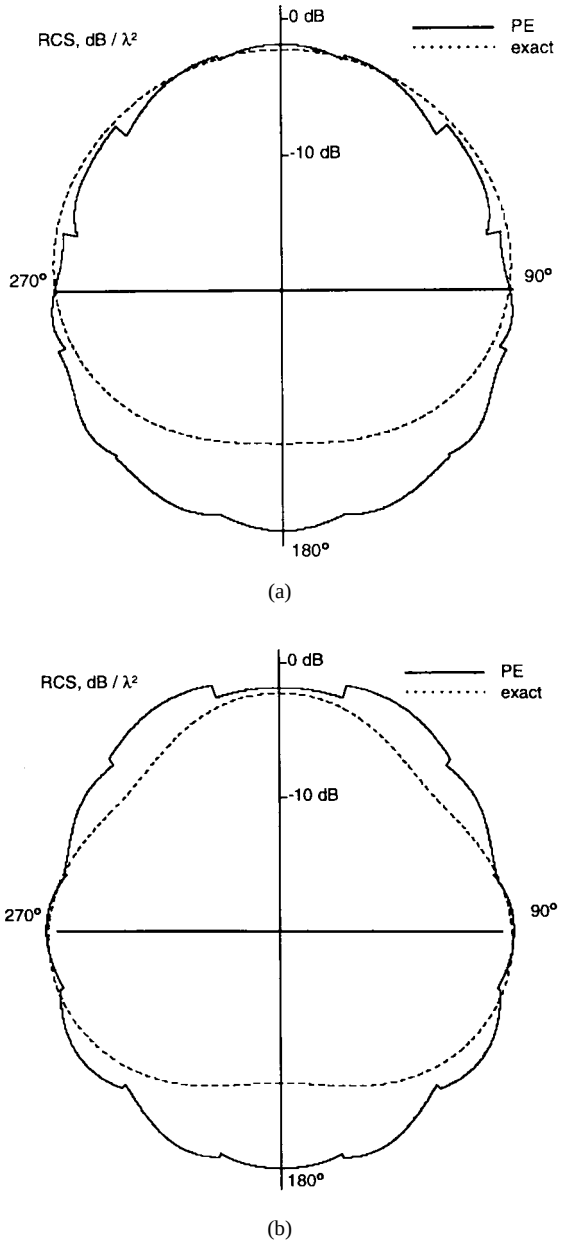

Fig. 10. Total bistatic RCS for perfectly conducting sphere of radius 0.25λ from seven rotated vector PE runs. (a) Horizontal plane pattern. (b) Vertical plane pattern.

When the size of the scatterer becomes comparable to the wavelength λ, the PE approximation becomes less accurate, as it neglects the effects of creeping waves which can propagate all around the object. This is illustrated in Fig. 10, which shows bistatic scattering results for a sphere of radius 0.25λ. The PE method breaks down except for forward scatter and 90° side scatter in the vertical plane, where the creeping wave cancels for reasons of symmetry. Parametric simulations show that results are reasonably accurate down to a radius of one wavelength.

Next, we consider the NASA almond (shown in Fig. 1), which is one of the most well-known test cases for scattering algorithms [13]. Because of the very flat shape of the almond and because published results are for the monostatic case (backscatter) only, this is a very stressful test for the PE method. For comparison purposes, computations were made with a backscatter physical optics (PO) code. For the backscatter case, the PO formulation simplifies to a scalar integral which is very fast to compute. The main drawback is that polarization effects are completely ignored by the PO approximation in the backscatter case.

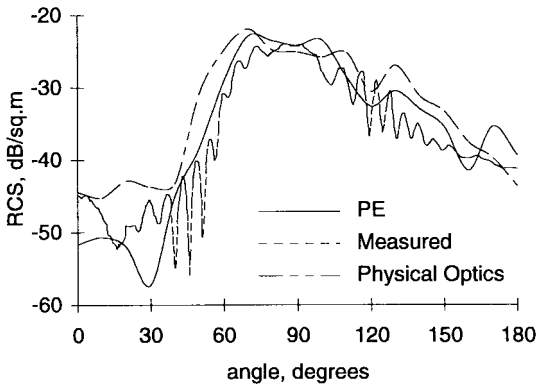

Fig. 11. Monostatic VV RCS of the NASA almond at 9.92 GHz as a function of azimuth angle. Almond length 9.936 in (25.237 cm).

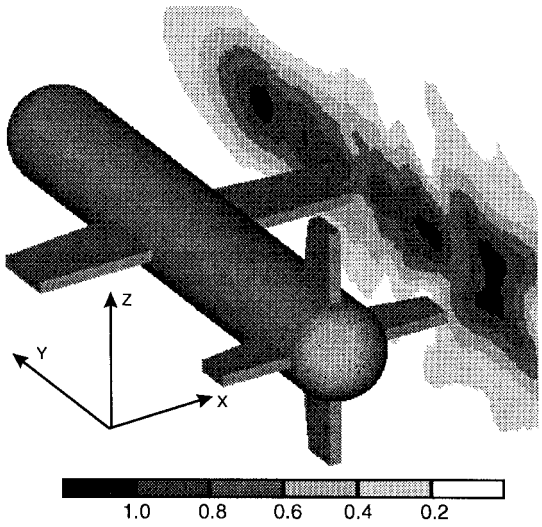

Fig. 12. Scattering by a 12-m-long idealized missile at 300 MHz. Amplitude of vertical (z) component of scattered electric field for the forward PE run. The incident wave has vertical polarization.

Fig. 11 shows the monostatic RCS of the NASA almond computed as a function of azimuthal angle for the case of vertical (VV) polarization. The frequency of the incident wave is 9.92 GHz and the almond length is 9.936 in (25.237 cm). The measured data was extracted from graphs published in [13]. The almond is measured with its broad side flat at zero elevation angle with 0° azimuth corresponding to incidence on the tip. Although both the PE and PO results roughly follow the measured data, they are not very accurate. As expected, the error decreases with azimuthal angle. When the almond is viewed from the side (90° azimuth), the models behave reasonably well, but the error increases substantially as incidence moves toward the tip of the almond where the creeping wave dominates. From this example, we can conclude that the accuracy of the PE and PO methods are comparable for the backscatter RCS calculations, although the PE is far more accurate for the forward scatter and the bistatic RCS modeling.

Finally, we use the vector PE with an idealized representation of a missile. The object is 12 m long and was made from

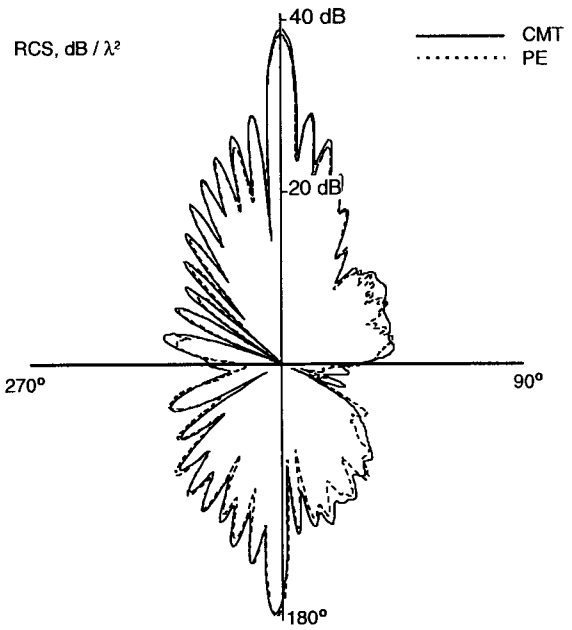

Fig. 13. Bistatic RCS in the horizontal plane for the 12-m-long idealized missile at 300 MHz.

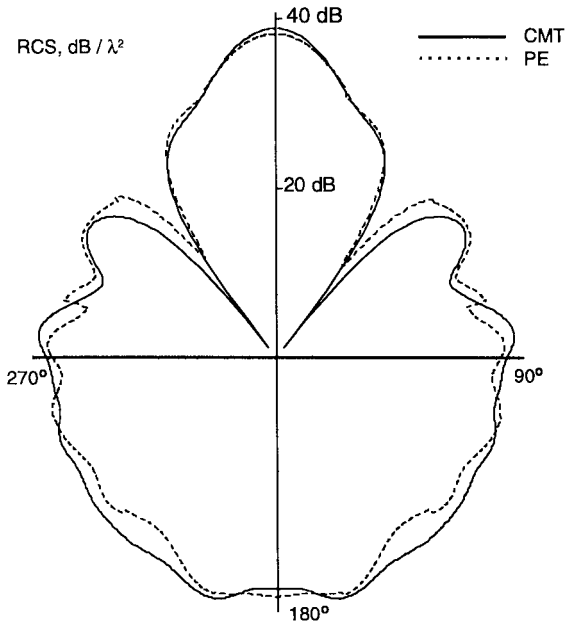

Fig. 14. Bistatic RCS in the vertical plane for the 12-m-long idealized missile at 300 MHz.

a 2-m-diameter cylinder with hemispherical caps and attached fins (Fig. 12). It should be noted here that the PE method does not require a decomposition of the target into canonically shaped elements and can deal directly with an arbitrary shaped target. Fig. 12 shows the amplitude of the vertical component of the scattered field computed for a vertically polarized (along the z-axis) incident wave propagated along the x-axis at a frequency of 300 MHz. The forward scattered field is shown just beyond the missile. Figs. 13 and 14 show bistatic RCS results in horizontal and vertical planes, the angles are

measured from the direction of the incident wave. We use the current marching technique (CMT) [14], [15] to validate the PE results. CMT is based on the magnetic field integral equation, which is solved with an efficient backward/forward iterative solver. The missile object was divided into 13618 triangles and we use the simplest pulse basis functions and delta functions as testing functions. The PE and CMT results are in good agreement. The vertical plane PE curve (Fig. 14) has larger errors compare to the horizontal plane data (Fig. 13). We believe that the main reason for the larger error in the vertical plane data is that the missile is quite thin (two wavelengths in diameter).

VII. Conclusions

The combination of the vector PE formulation with the rotated PE method provides a powerful tool for electromagnetic scattering calculations. The main limitation is that the paraxial framework cannot handle creeping waves accurately for objects with electrically small features. The bistatic RCS is computed from near-field results using appropriate near-field/far-field transformations. The full bistatic scattering pattern of a target can be reconstructed from a small number of narrow-angle vector PE runs. Both reflection and diffraction effects are automatically modeled, and polarization effects are fully taken into account. The examples given here demonstrate that the method can be applied to objects of a variety of sizes and shapes. The work presented here is limited to perfectly conducting objects embedded in a homogeneous background. Extension to the finite impedance case should be straightforward. Generalization to backgrounds with weak variations of the refractive index, for example involving tropospheric ducts, should be possible by coupling the vector PE with a long-range PE model [16].

Appendix

We want to prove that if the vector PE solution satisfies the divergence-free condition on the scatterer, then it does so everywhere in the domain outside the scatterer. In order to do this, we consider the function

$$f = \frac{i}{2k}\left(\frac{\partial^2 u_y^s}{\partial y^2} + \frac{\partial^2 u_z^s}{\partial z^2}\right) + iku_x^s + \frac{\partial u_y^s}{\partial y} + \frac{\partial u_z^s}{\partial z}. \quad \text{(A.1)}$$

It satisfies the SPE (5) and is zero on the initial transverse plane and on the boundary Σ of the scatterer. To show that it is zero everywhere outside the scatterer, we prove an energy conservation result.

Let u be a solution of (5) such that u and its partial derivatives up to order 2 are square integrable in each transverse plane and u is zero on Σ. Then the energy function

$$I(x) = \iint_{\Omega(x)} |u(x,y,z)|^2 \, dy \, dz \quad \text{(A.2)}$$

where $\Omega(x)$ is the intersection of the transverse plane at range x with the domain outside the scatterer does not depend on x.

Since f is zero on the initial transverse plane, its initial energy is zero. From the energy conservation result its energy function is zero everywhere, so f must be zero outside the scatterer as announced.

To prove the energy conservation results, we compute the derivative of the energy function

$$I'(x) = \iint_{\Omega(x)} \left(f\frac{\partial \overline{f}}{\partial x} \overline{f}\frac{\partial f}{\partial x}\right) dy \, dz + \lim_{h\to 0} \frac{1}{h} \iint_{\partial\Omega(x,h)} |f|^2 \, dy \, dz \quad \text{(A.3)}$$

where $\partial\Omega(x,h)$ is the increase in the transverse section of the scatterer between ranges x and $x+h$. Because f vanishes on the boundary of the scatterer, the limit on the RHS is zero. We now use the SPE to substitute for the range derivatives getting

$$I'(x) = \frac{i}{2k} \iint_{\Omega(x)} \left(f\left(\frac{\partial^2 \overline{f}}{\partial y^2} + \frac{\partial^2 \overline{f}}{\partial z^2}\right) - \overline{f}\left(\frac{\partial^2 f}{\partial y^2} + \frac{\partial^2 f}{\partial z^2}\right)\right) dy \, dz. \quad \text{(A.4)}$$

Note that the minus sign in the integrand in (A.4) is obtained because of the pure imaginary factor in the SPE formulation.

Applying Green's reciprocal theorem, we obtain

$$I'(x) = -\frac{i}{2k} \int_{\partial\Omega(x)} \left(f\frac{\partial \overline{f}}{\partial \vec{n}} - \overline{f}\frac{\partial f}{\partial \vec{n}}\right) ds \quad \text{(A.5)}$$

where $\vec{n}$ is the outer normal along the boundary $\partial\Omega(x)$ of $\Omega(x)$. Again, we use the fact that f vanishes on the boundary of the scatterer and, hence, on $\partial\Omega(x)$ to conclude that $I'(x) = 0$.

Acknowledgment

The authors would like to thank R. G. Haydon, Brasenose College, Oxford, U.K., for his help with the energy conservation aspects. They would also like to thank S. Rowlands, RAL, Chilton, U.K., for his help with implementation of the current marching technique.

References

[1] G. D. Dockery and J. R. Kuttler, "An improved impedance-boundary algorithm for Fourier split-step solutions of the parabolic wave equation," *IEEE Trans. Antennas Propagat.*, vol. 44, pp. 1592–1599, Dec. 1996.

[2] F. B. Jensen, W. A. Kuperman, M. B. Porter, and H. Schmidt, *Computational Acoustics*. New York: AIP, 1994.

[3] M. F. Levy and P.-P. Borsboom, "Radar cross-section computations using the parabolic equation method," *Electron. Lett.*, vol. 32, pp. 1234–1236, June 1996.

[4] M. F. Levy, P.-P. Borsboom, A. A. Zaporozhets, and A. Zebic-Le Hyaric, "RCS calculations with the parabolic wave equation," *AGARD Conf. Proc.*, Ankara, Turkey, Oct. 1996, no. 583, pp. 5.1–5.9.

[5] M. F. Levy and A. A. Zaporozhets, "Target scattering calculations with the parabolic equation method," *J. Acoust. Soc. Amer.*, vol. 103, pp. 735–741, Feb. 1998.

[6] K. R. Umashankar, "Numerical analysis of electromagnetic wave scattering and interaction based on frequency domain integral equation and method of moments technique," *Wave Motion*, vol. 10, pp. 493–525, Dec. 1988.

[7] A. Taflove, *Computational Electrodynamics: The Finite-Difference Time Domain Method*. Boston, MA: Artech House, 1995.

[8] M. Domingo, R. P. Torres, and M. F. Cátedra, "Calculation of the RCS from the interaction of edges and facets," *IEEE Trans. Antennas Propagat.*, vol. 42, pp. 885–888, June 1994.
[9] M. D. Collins, "A split-step Padé solution for the parabolic equation method," *J. Acoust. Soc. Amer.*, vol. 94, pp. 1736–1742, Apr. 1993.
[10] J.-P. Bérenger, "A perfectly matched layer for the absorption of electromagnetic waves," *J. Comput. Phys.*, vol. 114, pp. 185–200, Oct. 1994.
[11] C. Vassalo and F. Collino, "Highly efficient absorbing boundary conditions for the beam-propagation method," *J. Lightwave Technol.*, vol 14, pp. 1570–1577, June 1996.
[12] J. J. Bowman, T. B. A. Senior, and P. L. E. Uslenghi, *Electromagnetic Scattering by Simple Shapes*. New York: Hemisphere, 1987 (revised ed).
[13] H. T. G. Woo, M. J. Schuh, and M. L. Sanders, "Benchmark radar targets for the validation of computational electromagnetics programs," *IEEE Antennas Propagat. Mag.*, vol. 35, pp. 84–89, Feb. 1993.
[14] A. A. Zaporozhets and M. F. Levy, "Radar cross section calculation with marching methods," *Electron. Lett.*, vol. 34, no. 20, pp. 1971–1972, 1998.
[15] ———, "Current marching technique for electromagnetic scattering computations," *IEEE Trans Antennas Propagat*, vol. 47, pp. 1016–1024, June 1999.
[16] M. D. Collins and M. F. Werby, "A parabolic equation model for scattering in the ocean," *J. Acoust. Soc. Amer.*, vol. 85, pp. 1895–1902, May 1989.

Andrew A. Zaporozhets was born in Moscow, USSR, in 1965. He received the Master's and the Ph.D. degrees (physics and mathematics) from Moscow University, USSR, in 1988 and in 1991, respectively.

From 1992 to 1995, he was a Visiting Research Fellow at the University of Southampton, U.K., where he worked on fast synthesis techniques for shaped reflector antennas. Since 1996 he has been with the Rutherford Appleton Laboratory, Chilton, Didcot, U.K. His main area of research was in antennas for microwave power transmission. His current interests include marching techniques for the modeling of antennas, acoustical and radiowave propagation, and scattering.

Mireille F. Levy (M'96–SM'99) received the M.Sc. degree in mathematics from the University Paris 7 in 1976, and the Ph.D. degree in mathematics from the University Paris 6 in 1980.

Her initial career was as a mathematician at the University of Paris 6, France. In 1985 she joined the Radio Communications Research Unit, Rutherford Appleton Laboratory, Chilton, Didcot, U.K., where she is now in charge of the modeling group. She has worked on hybrid parabolic equation techniques for long-range radiowave applications, implementing models suitable for very large propagation domains. Her current activities focus on the development of marching methods for acoustic and electromagnetic scattering.

Dr. Levy is a member of the Institution of Electrical Engineers.